

Article

Detent Force Reduction of a C-Core Linear Flux-Switching Permanent Magnet Machine with Multiple Additional Teeth

Yi Du, Gang Yang, Li Quan *, Xiaoyong Zhu, Feng Xiao and Haoyang Wu

School of Electrical and Information Engineering, Jiangsu University, Zhenjiang 212013, China; duyie@ujs.edu.cn (Y.D.); 18852867835@163.com (G.Y.); zxyff@ujs.edu.cn (X.Z.); xiaofeng@ujs.edu.cn (F.X.); m18020484270@163.com (H.W.)

* Correspondence: quanli@ujs.edu.cn; Tel.: +86-511-88791266

Academic Editor: Chunhua Liu

Received: 10 January 2017; Accepted: 2 March 2017; Published: 7 March 2017

Abstract: C-core linear flux-switching permanent magnet (PM) machines (LFSPMs) are attracting more and more attention due to their advantages of simplicity and robustness of the secondary side, high power density and high torque density, in which both PMs and armature windings are housed in the primary side. The primary salient tooth wound with a concentrated winding consists of C-shaped iron core segments between which PMs are sandwiched and the magnetization directions of these PMs are adjacent and alternant in the horizontal direction. On the other hand, the secondary side is composed of a simple iron core with salient teeth so that it is very suitable for long stroke applications. However, the detent force of the C-core LFSPM machine is relatively high and the magnetic circuit is unbalanced due to the end effect. Thus, a new multiple additional tooth which consists of an active and a traditional passive additional tooth, is employed at each end side of the primary in this paper, so that the asymmetry due to end effect can be depressed and the detent force can be reduced by adjusting the passive additional tooth position. By using the finite element method, the characteristics and performances of the proposed machine are analyzed and verified.

Keywords: flux-switching permanent magnet (FSPM) machine; linear machine; detent force reduction

1. Introduction

Cableless elevator systems based on linear machines are very attractive, since they can eliminate the drawbacks of conventional traction-gear cable elevators, such as the vertical oscillation and height limit caused by the strength and weight of cable [1], especially in case of the skyscrapers of 200–400 m height. Moreover, multicar elevators in one hoistway can be achieved more easily when the elevator vehicles are driven by independent linear machines [2], so a large proportion of the building space can be reclaimed. Hence, several kinds of linear machines have been investigated for cableless elevators. In [3], a linear permanent magnet (PM) synchronous machine (LPMSM) is adopted for cableless elevators because of its high efficiency and high power density, in which the armature windings are laid along the hoistway and can be controlled section by section according to the elevator vehicle position. PMs are installed on the elevator vehicle. However, the cost of LPMSM is very high because of the long laid armature windings and the expensive power electronic equipment used to divide the armature windings into sections. Due to the simplicity and robustness of the secondary side, the linear switched reluctance machine (LSRM) is regarded as the preferred machine for cableless elevators [4]. However, the thrust force ripple of LSRMs is relatively higher due to the complex and nonlinear magnetic circuit and the control difficulty of LSRM is consequently increased [5].

In recent years, stator PM machines, namely the double salient PM (DSPM) machine, flux reverse PM (FRPM) machine and flux-switching PM (FSPM) machine have been widely investigated because of

their advantages such as the simple and robust structure of the rotor [6,7]. Both the PMs and armature windings of stator PM machines are housed in the stator, and the rotor is composed of a simple and cheap iron core with salient teeth, so the linear counterpart of the stator PM machine, namely the linear primary PM machine, is very suitable for long stroke applications, such as cableless elevators and urban rail transit systems, in which the primary and the secondary can be designed as the short side and long side, respectively, to integrate the high efficiency and power density performances of LPMSMs and the low cost merit of LSRMs.

Compared with the DSPM machine and the FRPM machine, the FSPM machine possesses the merits of higher power density and torque density [8], sinusoidal no-load EMF [9] and fault-tolerance capability [10–14], so FSPMs are attracting more and more attention and numerous novel rotary FSPM machines structures of have been proposed [15,16], such as the five-phase modular FSPM machine [17] and the hybrid excitation FS machine [18]. Meanwhile lots of linear versions of FSPM (LFSPM) machines also have been presented for linear industry applications [19]. In [20], E-core and C-core LFSPM machines were optimized and compared. Due to the improvement of the armature winding slot area compared with traditional U-core LFSPM machines, the C-core LFSPM machines can achieve a higher thrust force density and power density, in spite of the lesser usage of the PMs.

However, the performances of LFSPM machines, including U-core, E-core and C-core LFSPM machines are usually severely deteriorated due to the asymmetrical characteristics of the magnetic field as a result of the end effect, although two additional teeth can be added on the each end of the primary side. In order to obtain the symmetrical 3-phase flux linkage and no-load EMF, a complementary and modular E-core LFSPM machine is proposed for urban rail transit and the corresponding mathematical model is established [21].

In this paper, a C-core LFSPM machine with two new multiple additional teeth is proposed for cableless elevator direct drive systems. As shown in Figure 1, two LFSPM machines are located in the two gaps, respectively, between the hoistway and the elevator vehicle to achieve a balanced lifting force. The primary side is installed on the outside of the elevator car and the secondary side is laid along the hoistway. In Section 2, the machine configuration will be described and the operation principle will be introduced briefly. Then, the key parameters of the proposed machine will be optimized to achieve balanced electromagnetic performances and low detent force in Section 3. In Section 4, the characteristics of the C-core LFSPM machine will be analyzed by the 2-D finite element method (FEM). Finally, conclusions will be drawn in Section 5.

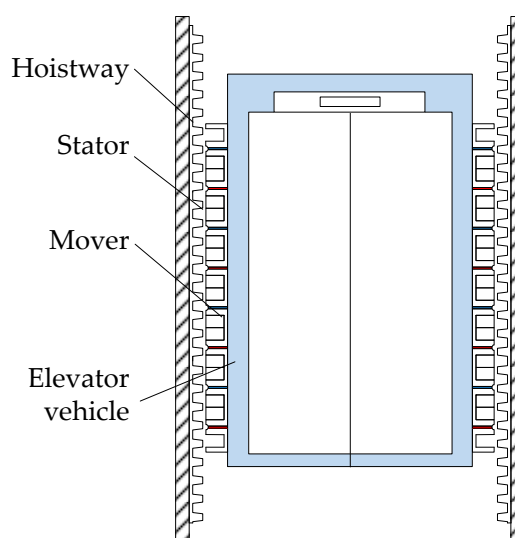


Figure 1. Direct drive elevator system.

2. Machine Configuration and Operation Principle

The performance and characteristics of LFSPM machines have been widely investigated. Figure 2a shows an original C-core LFSPM machine, named “Machine I” in this paper, which can be obtained by splitting a rotary 6/13-pole C-core FSPM machine along the radial direction and unrolling it. It should be notice that the 6/13 mover and stator pole combination is selected in this paper because it can achieve the maximum no-load EMF and thrust force [20].

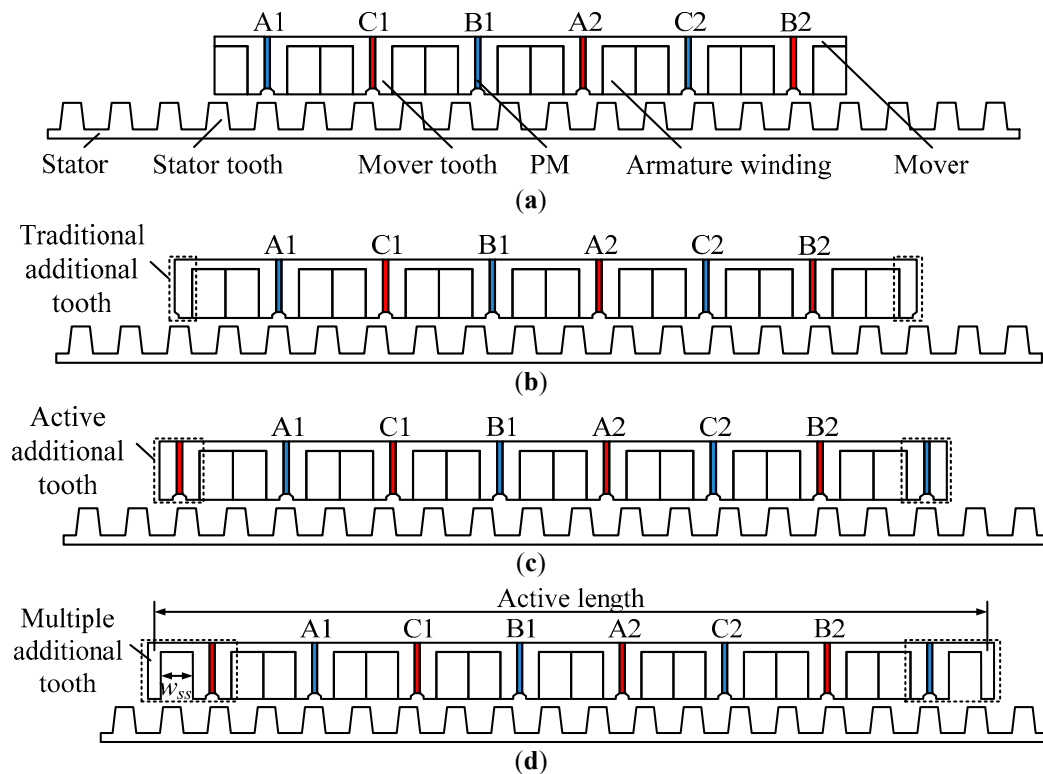


Figure 2. C-core linear flux-switching permanent magnet machine configurations. (a) Without additional tooth, Machine I; (b) with traditional passive additional tooth, Machine II; (c) with active additional tooth, Machine III; (d) with multiple additional tooth, Machine IV.

Figure 3 shows the operation principle of the 6/13-pole C-core LFSPM machine. Assuming the PM magnetizes towards the left-hand side, at the relative position of the stator tooth and the mover tooth as shown in Figure 3a, the PM flux linkage of the coil nearly reaches the positive maximum. When the mover moves a quarter of the tooth pitch towards the left-hand side, as shown in Figure 3b, the mover module is symmetrical about the central axis of the stator slot. At this moment, the PM flux linkage of the coil equals zero. When the mover moves 1/4 tooth pitch again, as shown in Figure 3c, the PM flux linkage nearly reaches the negative maximum value. In Figure 3d, the mover module is symmetrical about the central axis of the stator tooth. Thus the PM flux linkage of the coil equals zero again. Assuming an ideally sinusoidal PM flux linkage, Figure 3e shows the PM flux linkage waveform when the mover travels one stator tooth pitch, in which positions A, B, C and D correspond to the positions in Figure 3a–d, respectively.

In order to reduce the detent force, two passive additional teeth are adopted [22] in a U-core LFSPM machine and the width of the side-slot has been optimized for the minimum detent force. Thus, the traditional passive additional teeth also can be employed in the C-core LFSPM machine, as shown in Figure 2b, which is named as “Machine II” in this paper, to reduce the detent force. However, the other electromagnetic performances, such as the flux linkage and the inductance, are unbalanced due to the end effect of the linear machine not only in the Machine I but also in the Machine II.

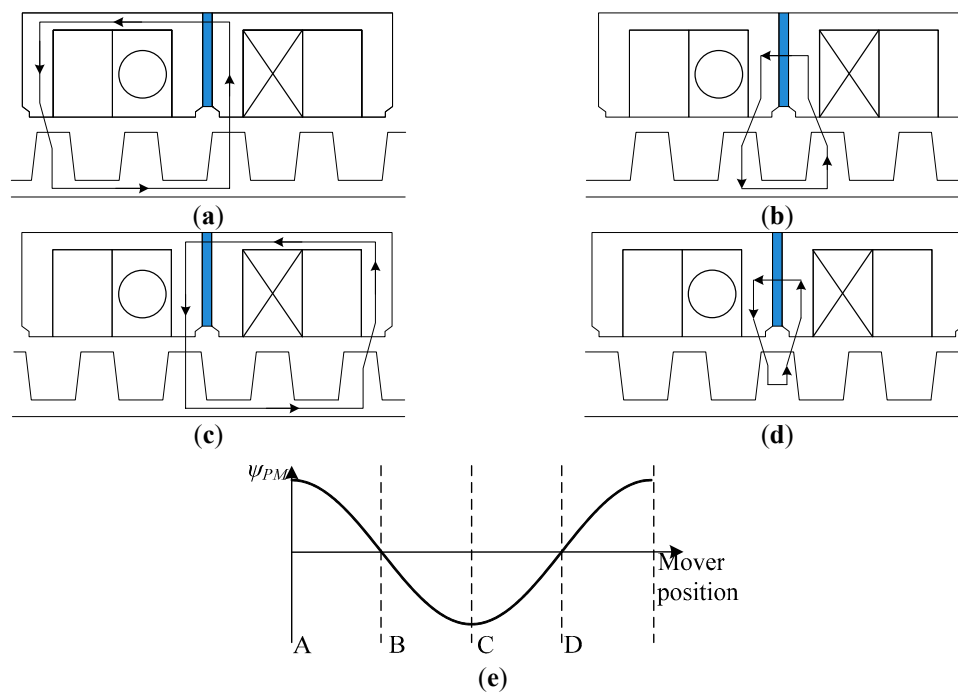


Figure 3. Operation principle of 6/13-pole C-core LFSPM machine. (a) Position A; (b) Position B; (c) Position C; (d) Position D; (e) Ideal coil PM flux linkage.

In this paper, 2-D FEM models of the four machines shown in Figure 2 have been built. Thus the machine characteristics can be obtained. Figure 4 shows the 3-phase PM flux linkage waveforms of Machine I and Machine II. It can be seen that the flux linkage waveforms of Machine I are asymmetrical in the positive and negative half-cycle. Furthermore, the flux linkage waveforms of Machine II are more deteriorated compared with those of Machine I due to the magnetic circuit of the traditional additional teeth.

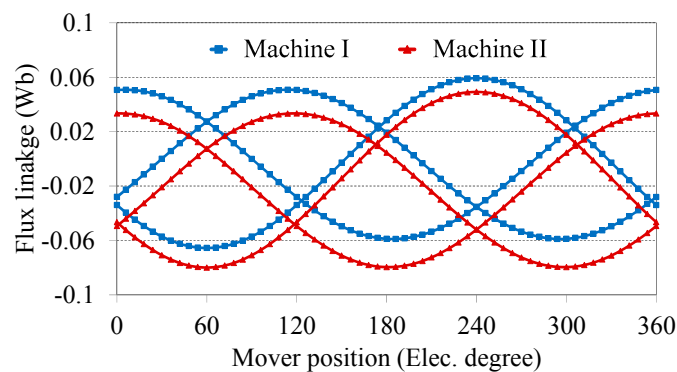


Figure 4. 3-phase PM flux linkage waveforms of Machine I and Machine II.

In order to balance the magnet circuit, two active additional teeth [23] are added at each end of the primary side of Machine I, as shown in Figure 2c, which is named as Machine III in this paper. It can be noticed that the active additional tooth is composed of two primary tooth iron cores and a PM block. Figure 5 shows the no-load magnetic field distribution of Machine III. It can be seen that the flux contributed by the active additional tooth runs through the mover teeth, thus balancing the magnetic field asymmetry caused by the end effect of the linear machine. The 3-phase flux linkage waveforms of Machine III are expected to be more balanced than the other two counterparts. As shown in Figure 6, the 3-phase flux linkage waveforms are nearly symmetrical in the positive and negative half-cycle.

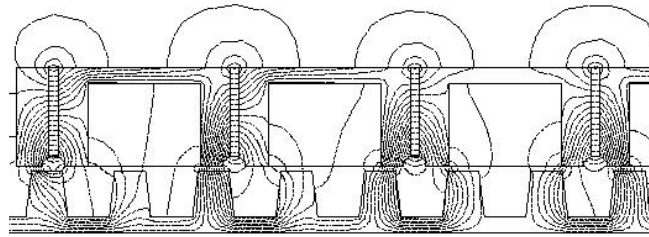


Figure 5. No-load magnetic field distribution of Machine III.

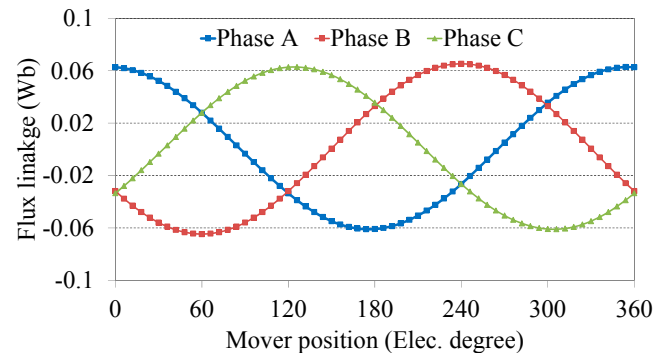


Figure 6. 3-phase flux linkage waveforms of Machine III.

The merit of the traditional passive additional teeth in Machine II is that the detent force can be optimized through adjusting the width of the side-slot. However, the side slot width cannot be changed arbitrarily in Machine III, which will deteriorate the phase and the amplitude of the flux linkage and no-load EMF, especially of phase A and phase B which are arranged to be close to the additional teeth, so a new multiple additional tooth, which is composed of an active additional tooth and a traditional passive tooth, is employed in the C-core LFSPM machine. As shown in Figure 2d, in the proposed C-core LFSPM, which is named as Machine IV, both the PMs and armature windings are located in the primary side. The primary salient tooth wound with a concentrated winding consists of C-shaped laminated segments between which the PMs are sandwiched and the magnetization directions of these PMs are adjacent alternant in horizontal direction. And the secondary side is composed of a simple iron core with salient teeth so that it is very suitable to be used in long stroke applications, such as cableless elevators. Due to the use of two multiple additional teeth, the magnet circuit can be balanced and the detent force can be optimized through adjusting the width of the side slot, w_{ss} .

3. Key Parameter Optimization

The proposed LFSPM machine with multiple additional teeth is operated based on the flux switching principle, which is same as the conventional FSPM machine. In this section, several key parameters will be optimized using the FEM in order to obtain the expected performances, such as the symmetry and sinusoidal 3-phase flux linkage and no-load EMF waveforms, the minimum detent force and the maximum average thrust force. It should be noted that the mover tooth tip width b_{mtt} and the slot under the PM b_{sPM} are designed to be equal to the one-eighth of the mover pitch τ_m in the optimization process, as shown in Figure 7, which is similar with the traditional FSPM machine [9], thus the mover slot width b_{ms} equals 5/8 times τ_m , namely $b_{mtt} = b_{sPM} = 1/8\tau_m = 1/5b_{ms}$.

Moreover, the individual parameter optimization method [20] is adopted in the key parameter optimization. On the other hand, the magnetic flux density is considered to ensure the iron core to be unsaturation.

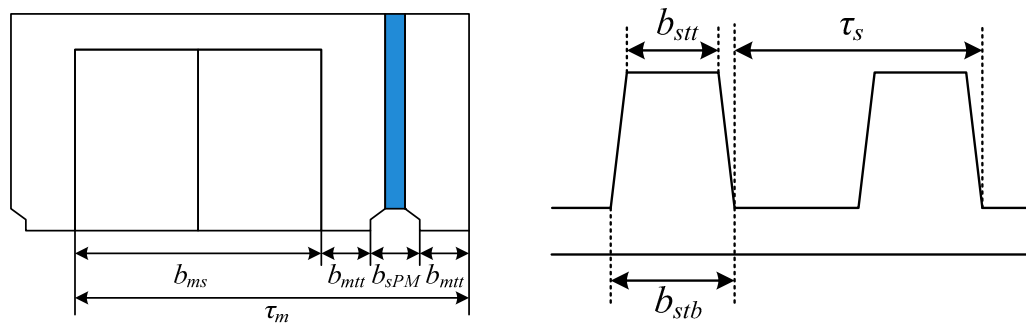


Figure 7. Definition of key parameters.

As shown in Figure 8, due to the passive additional teeth, the flux density values in the secondary side yoke nearby the two end teeth of primary side in Machine II and Machine IV are obviously higher than those in Machine I and Machine III.

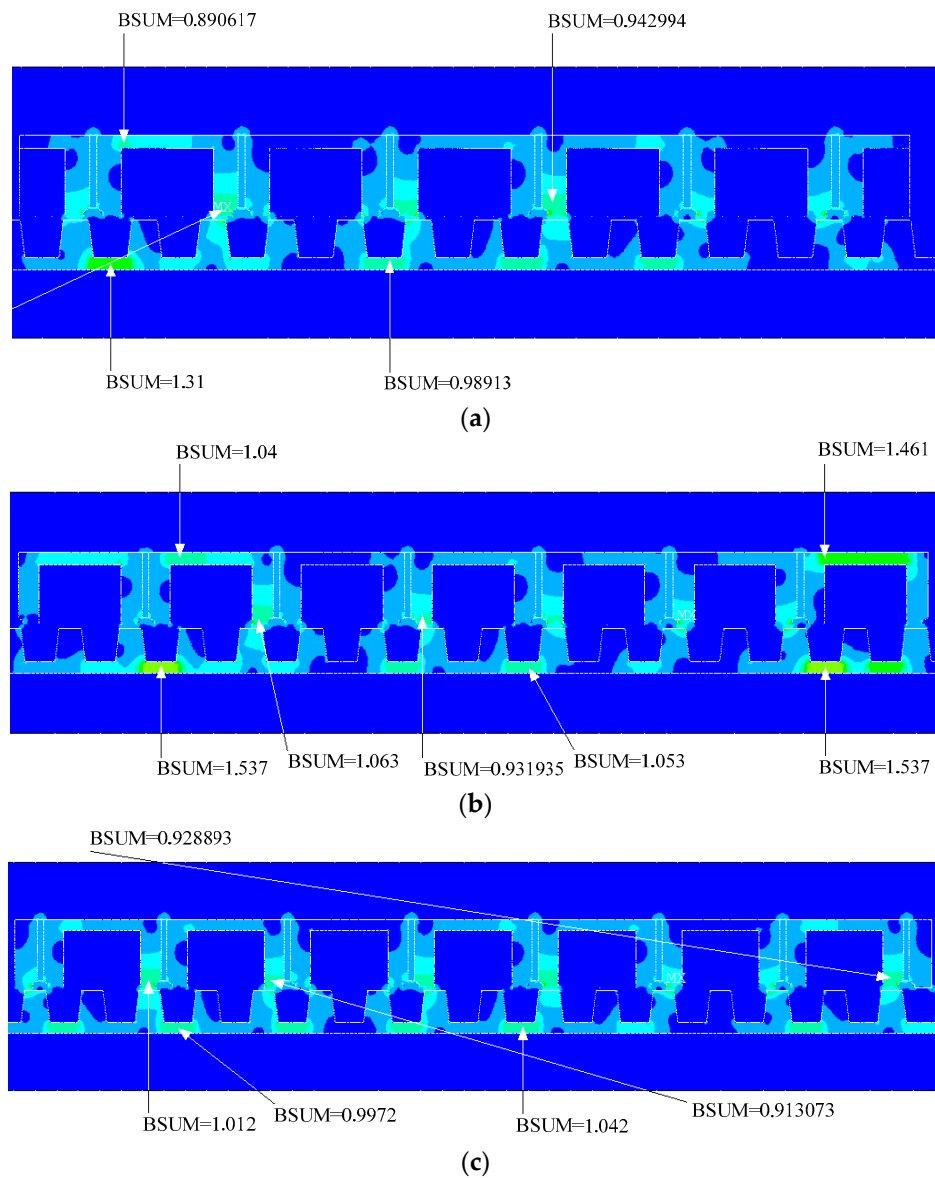


Figure 8. Cont.

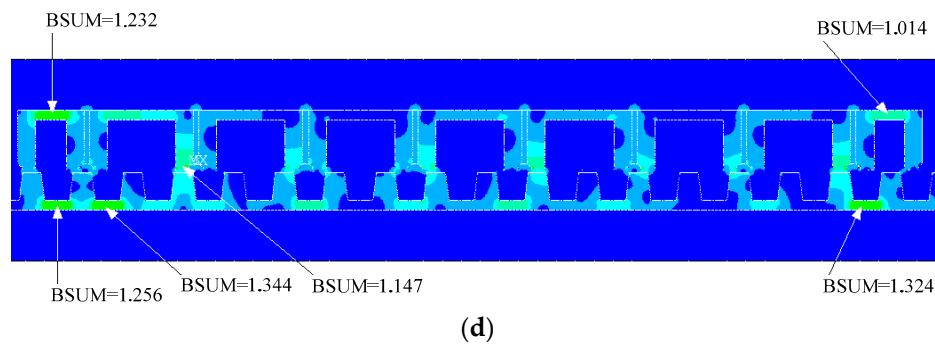


Figure 8. Magnetic flux density distribution. (a) Machine I; (b) Machine II; (c) Machine III; (d) Machine IV.

3.1. Width of Stator Teeth

First of all, the width of the stator (the secondary side) tooth tip and tooth root, which are shown in Figure 7, are optimized. Figure 9 shows the detent force peak-to-peak value of the proposed machine with different c_{stt} and c_{stb} , where c_{stt} is defined as the ratio of the width of stator tooth tip b_{stt} to the stator tooth pitch τ_s , and c_{stb} is defined as the ratio of the width of stator tooth root b_{stb} to the stator tooth pitch τ_s . It can be found that the detent force achieves the minimum value when c_{stt} and c_{stb} equal 0.39 and 0.55, respectively. Actually, c_{stb} does not have a significant effect on the detent force.

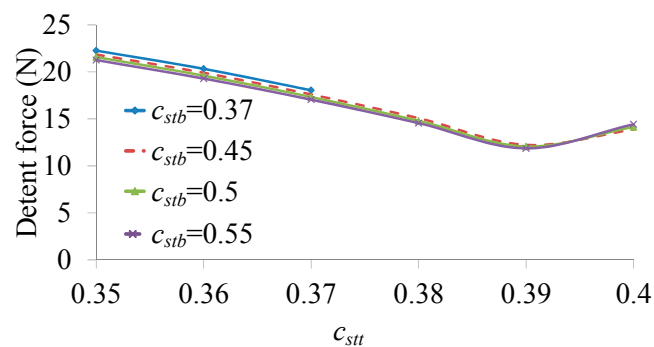


Figure 9. Detent force peak-to-peak value with different c_{stt} and c_{stb} .

Figure 10 shows the change of the no-load EMF THD with respect to c_{stt} and c_{stb} . It indicates that the no-load EMF THD increases with the rise of c_{stt} . And, the no-load EMF THD is not sensitive to c_{stb} either.

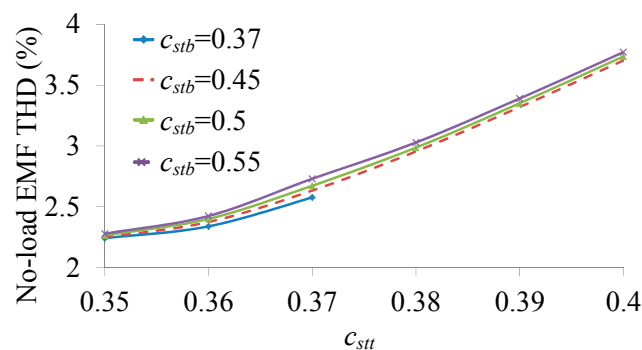


Figure 10. THD of no-load EMF with different c_{stt} and c_{stb} .

Consequently, the no-load EMF peak-to-peak values with the different c_{stt} and c_{stb} are calculated. As shown in Figure 11, the no-load EMF peak-to-peak value reduces with respect to the increase of c_{stt} and c_{stb} , due to the flux leakage around the stator teeth.

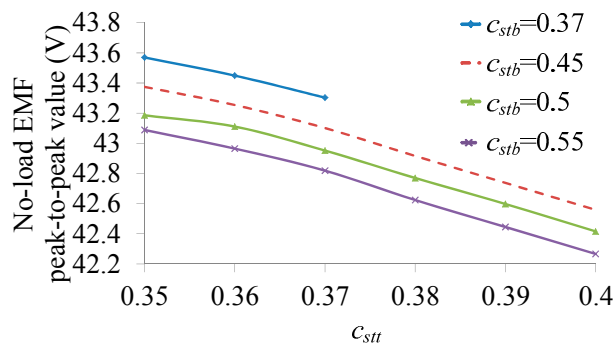


Figure 11. No-load EMF peak-to-peak value with different c_{stt} and c_{stb} .

Based on Figures 10 and 11, a conclusion can be drawn that the better performances of no-load EMF can be achieved when the relatively smaller c_{stt} and c_{stb} are adopted. However, the excessive narrow stator teeth will result in serious magnetic saturation when the currents are fed into the armature windings. Thus the thrust force will be restrained and the efficiency of the machine will be reduced. So, the thrust force has to be analyzed to obtain the optimal c_{stt} and c_{stb} values taking into account the magnetic field in iron core caused by both of the armature current and the PMs.

Figure 12 shows the average thrust force values with the different c_{stt} and c_{stb} . It can be found that the thrust force improves firstly and then reduces with the increase of c_{stt} , and reduces with the increase of c_{stb} . When $c_{stt} = 0.37$ and $c_{stb} = 0.37$, the thrust force achieves the maximum value which is equal to be about 225 N.

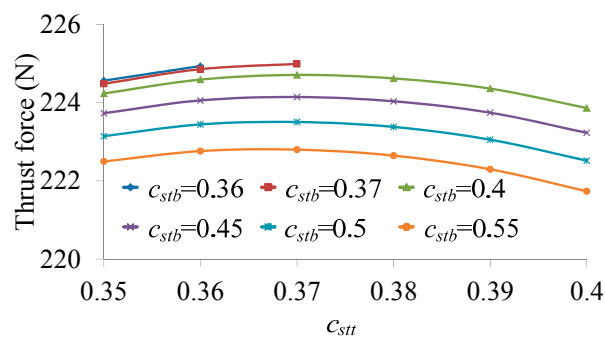


Figure 12. Average thrust force value with different c_{stt} and c_{stb} .

3.2. Width of Side Slot

The multiple additional tooth is composed of an active additional tooth and a traditional passive additional tooth. And the width of the side-slot, which is between the active additional tooth and the passive additional tooth, can be adjusted to optimize the detent force of the C-core LFSPM machine. As shown in Figure 2d, the width of the side-slot is defined as:

$$w_{mss} = c_{ss} \tau_s, \quad (1)$$

where w_{mss} is the width of the side-slot, τ_s is the pitch of the stator tooth and c_{ss} is the ratio between w_{mss} and τ_s .

Figure 13 shows the detent force waveforms versus c_{ss} when $c_{stt} = 0.37$ and $c_{stb} = 0.5$. And the peak-to-peak values with the different c_{ss} are listed in Table 1. It can be seen that the detent force

peak-to-peak value changes versus c_{ss} . When $c_{ss} = 0.625$, as listed using italic numbers, the detent force peak-to-peak value can achieve the minimum value which is 38.3% of that of Machine III.

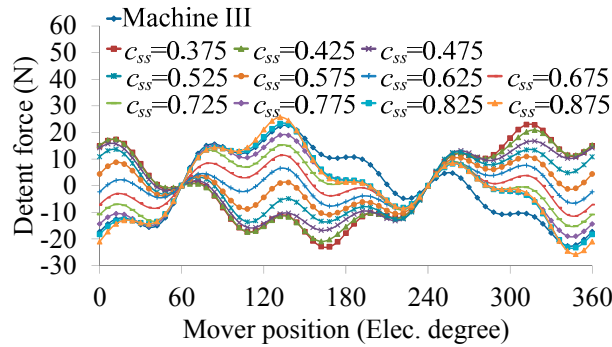


Figure 13. Detent force waveforms with different c_{ss} .

Table 1. Side-slot width and machine active length with different c_{ss} .

c_{ss}	w_{ss} (mm)	L_a (mm)	L_a/τ_s	Detent Force Peak-to-Peak Value (N)
Machine III	/	295	≈ 15.6	45.24
0.375	6.923	313.846	17.0	45.88
0.425	7.846	315.692	17.1	41.86
0.475	8.769	317.538	17.2	33.54
0.525	9.692	319.385	17.3	27.22
0.575	10.615	321.231	17.4	21.87
0.625	11.538	323.077	17.5	17.32
0.675	12.462	324.923	17.6	22.78
0.725	13.385	326.769	17.7	30.45
0.775	14.308	328.615	17.8	38.01
0.825	15.231	330.462	17.9	46.61
0.875	16.154	332.308	18.0	51.47

Defining the active length of the proposed machine as the distance between the midlines of the two passive additional teeth, the active length of the proposed machine can be expressed as:

$$L_a = 7\tau_m + 2w_{mt} + w_{PM} + w_{mst} + 2w_{mss}, \quad (2)$$

where w_{mt} , w_{PM} and w_{mst} are the width of the mover tooth, the width of the PM and the width of passive additional tooth, respectively, τ_m is the pitch of the mover tooth, and L_a is the active length of the proposed machine. Consequently, the width of the side-slot and the active length of the proposed machine can be obtained according to the dimension parameters. As listed in Table 1, when $c_{ss} = 0.625$, the detent force peak-to-peak value equals 17.32 N, and the width of the side-slot and the active length of the proposed machine are equal to 11.538 mm and 323.077 mm, respectively. It should be noticed that the ratio between L_a and τ_s is 17.5. In fact, the detent force of the PM linear machine is composed of two components, namely, the slot effect and the end effect. And the adjustment of the width of side-slot is mainly to reduce the end effect detent force. When the active length of the short side of the LFSPM machine equals odd times of half of the stator tooth pitch, the phase difference of the two end effect detent force components caused by each end, respectively, equals 180° . Thus the resultant end effect detent force can be minimized, which is consistent with the FEM result.

4. Electromagnetic Performance Analysis

Based on the optimization design, a 3-phase 6/13-pole C-core LFSPM machine with the multiple teeth is designed. The corresponding key parameters are listed in Table 2. Then the static characteristics of the proposed machine are analyzed by using the FEM.

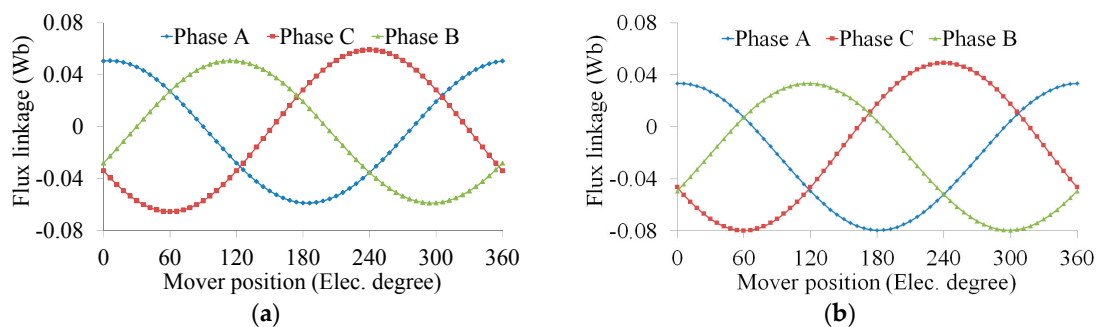
Table 2. Key parameters of the proposed machine.

Parameter	Value	Parameter	Value
Pitch of mover tooth, τ_m (mm)	40	c_{ss}	0.625
Pitch of mover tooth, τ_s (mm)	240/13	c_{sst}	0.37
Width of mover tooth, w_{mt} (mm)	6.5	c_{stb}	0.37
Width of passive additional tooth, w_{mst} (mm)	5	Winding number per phase (turn)	180
Width of PMs, w_{PM} (mm)	2	PM remanence (T)	1.2
Width of side-slot, w_{mss} (mm)	11.538	PM material	N35M
Airgap length (mm)	1	Iron core material	50W350

Figure 14 shows the 3-phase no-load flux linkage waveforms of four machines. It can be seen that flux linkage peak-to-peak values of Machine III and Machine IV are obviously improved compared with those of the other machines due to the contribution of the active additional teeth PMs. Machine II exhibits the maximum DC components and the most serious asymmetry in its 3-phase flux linkage peak-to-peak values. Furthermore, the asymmetry of Machine IV is effectively restrained, although the DC components are a little bigger than those of Machine I and Machine III. In order to indicate the improvement clearly, the key parameters of the no-load flux linkage are listed in Table 3.

Table 3. No-load flux linkage values (mWb).

Machine No.	Parameters	Phase A	Phase B	Phase C
Machine I	Positive max.	50.82	50.83	59.28
	Negative max.	-58.90	-58.90	-65.52
	P-P value	109.71	109.73	124.80
	DC component	-3.28	-4.56	-3.44
Machine II	Positive max.	33.41	33.41	49.22
	Negative max.	-79.60	-79.60	-79.91
	P-P value	113.01	113.01	129.13
	DC component	-21.73	-23.09	-15.27
Machine III	Positive max.	62.81	62.81	65.28
	Negative max.	-61.02	-61.01	-64.71
	P-P value	123.82	123.82	129.99
	DC component	1.88	0.31	-0.08
Machine IV	Positive max.	72.00	71.99	69.06
	Negative max.	-56.49	-56.48	-58.90
	P-P value	128.48	128.48	127.96
	DC component	8.43	6.79	4.40

**Figure 14.** Cont.

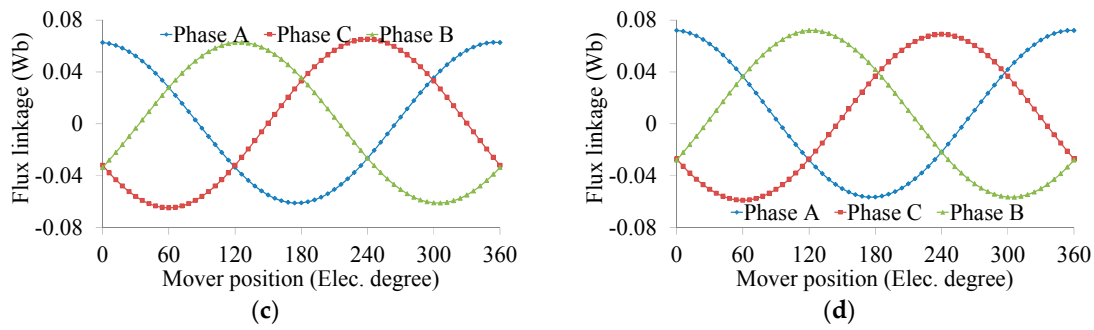


Figure 14. 3-phase no-load flux linkage waveforms. (a) Machine I; (b) Machine II; (c) Machine III; (d) Machine IV.

Then the no-load EMF can be obtained by differentiating the flux linkage with respect to time. As shown in Figure 15, the no-load EMF waveforms of machine IV are also very symmetrical, and the peak-to-peak values of the 3-phase are 43.3 V, 43.1 V and 43 V, respectively.

When the $i_d = 0$ control strategy is adopted, namely, the armature currents are in phase with the 3-phase no-load EMF, the thrust force can be calculated. Figure 16 shows the thrust force waveforms of four machines. The detent force waveforms are plotted in Figure 17.

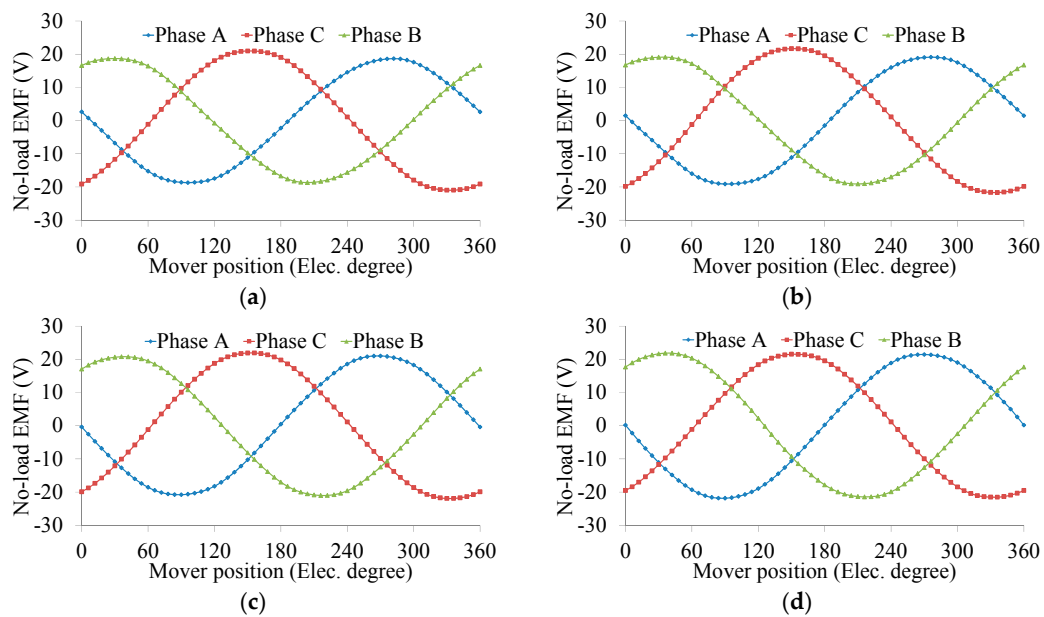


Figure 15. 3-phase no-load EMF waveforms. (a) Machine I; (b) Machine II; (c) Machine III; (d) Machine IV.

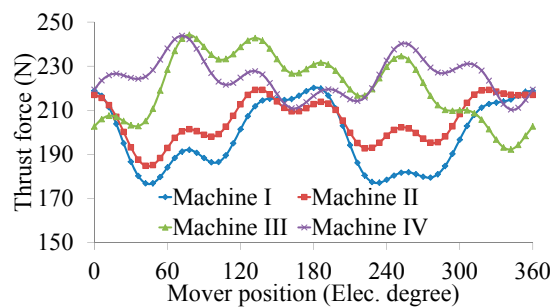


Figure 16. Thrust force comparison among four machines.

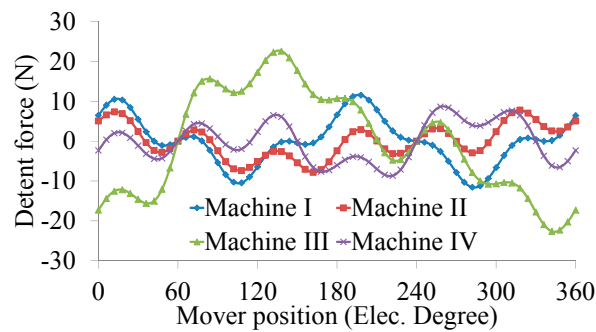


Figure 17. Detent force comparison among four machines.

The corresponding values are compared in Table 4. It can be seen that Machine IV can achieve the maximum average value and the minimum peak-to-peak value of thrust force. Although the detent force peak-to-peak value of Machine II is a little smaller than that of Machine IV, the thrust ripple is higher than that of Machine IV. The peak-to-peak value of the detent force of Machine IV is 17.32 N, which is less than 8% of the average thrust force.

Table 4. Thrust force and detent force values (N).

Machine No.	Parameters	Thrust Force	Detent Force
Machine I	Average value	198.39	/
	P-P value	43.27	23.13
	Ratio	21.80%	11.66%
Machine II	Average value	205.50	/
	P-P value	34.48	15.60
	Ratio	16.78%	7.59%
Machine III	Average value	220.87	/
	P-P value	51.91	45.24
	Ratio	23.50%	20.49%
Machine IV	Average value	224.99	/
	P-P value	33.47	17.32
	Ratio	14.88%	7.70%

5. Conclusions

In this paper, a C-core LFSPM machine is proposed for long stroke applications such as cableless elevators. The key of the proposed machine is that two multiple additional teeth are employed at each end of the mover side. The multiple additional teeth are composed of an active additional tooth and a traditional passive additional tooth, in which the function of the active additional tooth is to balance the asymmetric 3-phase magnetic circuit due to the end effect, and the passive additional tooth contributes to reduce the detent force through adjusting the width of side-slot. Based on FEM analysis, the width of stator tooth and the width of side-slot are optimized to achieve high thrust force, low detent force, high no-load EMF THD, and so on. Finally, the average thrust force of 224.99 N and the detent force peak-to-peak value of 17.32 N of proposed machine can be achieved. It should be mentioned that Machine IV possesses the minimum thrust force ripple of 14.88% and the most balanced 3-phase no-load flux linkage among the four machines. It confirms that the end effect of proposed machine is restricted greatly due to multiple additional teeth. However, the thrust force ripple is still high for the stable operation of elevator due to the double tooth structure of FSPM machines, so suitable control strategies, such as the harmonic current injection method can be adopted to provide a lower thrust force ripple. The prototype machine and its experiment results will be presented in a future paper.

Acknowledgments: This work was supported and funded in part by grants (Project No. 51677081 and 51307072) from the National Natural Science Foundation of China, the grant from the priority academic program development of Jiangsu higher education institution and the Program for Postgraduate Research Innovation in General Universities of Jiangsu Province 2014 under Project KYLX_1047.

Author Contributions: Yi Du is the main author of this manuscript who implemented the research and performed the analysis. Li Quan and Xiaoyong Zhu conceived of the idea of the research and provided guidance. Gang Yang, Feng Xiao and Haoyang Wu provided some useful suggestions in the construction of this paper. All the authors have contributed significantly to this work.

Conflicts of Interest: The authors declare no conflict of interest.

References

1. Ishii, T. Elevators for skyscrapers. *IEEE Spectr.* **1994**, *31*, 42–46. [[CrossRef](#)]
2. Onat, A.; Kazan, E.; Takahashi, N.; Miyagi, D.; Komatsu, Y.; Markon, S. Design and implementation of a linear motor for multicar elevators. *IEEE/ASME Trans. Mechatron.* **2010**, *15*, 685–693. [[CrossRef](#)]
3. Wang, X.; Feng, H.; Xu, B.; Xu, X. Research on permanent magnet linear synchronous motor for rope-less hoist system. *J. Comput.* **2012**, *7*, 1361–1368. [[CrossRef](#)]
4. Lim, H.S.; Krishan, R. Ropeless elevator with linear switched reluctance motor drive actuation systems. *IEEE Trans. Ind. Electron.* **2007**, *54*, 2209–2218.
5. Zhao, S.W.; Cheung, N.C.; Gan, W.; Yang, J.M.; Pan, J.F. A self-tuning regulator for the high-precision position control of a linear switched reluctance motor. *IEEE Trans. Ind. Electron.* **2007**, *54*, 2425–2434. [[CrossRef](#)]
6. Cheng, M.; Hua, W.; Zhang, J.Z.; Zhao, W.X. Overview of stator-permanent magnet brushless machines. *IEEE Trans. Ind. Electron.* **2011**, *58*, 5087–5101. [[CrossRef](#)]
7. Du, Y.; Chau, K.T.; Cheng, M.; Fan, Y.; Wang, Y.B.; Hua, W.; Wang, Z. Design and analysis of linear stator permanent magnet vernier machines. *IEEE Trans. Magn.* **2011**, *47*, 4219–4222. [[CrossRef](#)]
8. Hua, W.; Zhu, Z.Q.; Cheng, M.; Pang, Y.; Howe, D. Comparison of flux-switching and doubly-salient permanent magnet brushless machines. In Proceedings of the 2005 IEEE International Conference on Electrical Machines and Systems (ICEMS), Nanjing, China, 27–29 September 2005; pp. 165–170.
9. Hua, W.; Cheng, M.; Zhu, Z.Q.; Howe, D. Analysis and optimization of back EMF waveform of a flux-switching permanent magnet motor. *IEEE Trans. Energy Convers.* **2008**, *23*, 727–733. [[CrossRef](#)]
10. Zhao, W.X.; Cheng, M.; Hua, W.; Jia, H.Y.; Cao, R.W. Back-EMF harmonic analysis and fault-tolerant control of flux-switching permanent-magnet machine with redundancy. *IEEE Trans. Ind. Electron.* **2011**, *58*, 1926–1935. [[CrossRef](#)]
11. Zhao, W.X.; Cheng, M.; Chau, K.T.; Hua, W.; Jia, H.Y.; Ji, J.H.; Li, W.L. Stator-flux-oriented fault-tolerant control of flux-switching permanent-magnet motors. *IEEE Trans. Magn.* **2011**, *47*, 4191–4194. [[CrossRef](#)]
12. Zhao, W.X.; Cheng, M.; Cao, R.W.; Ji, J.H. Experimental comparison of remedial single-channel operations for redundant flux-switching permanent-magnet motor drive. *Prog. Electromagn. Res.* **2012**, *123*, 189–204. [[CrossRef](#)]
13. Zhao, W.X.; Cheng, M.; Chau, K.T.; Chan, C.C. Control and operation of fault-tolerant flux-switching permanent-magnet motor drive with second harmonic current injection. *IET Electr. Power Appl.* **2012**, *6*, 707–715. [[CrossRef](#)]
14. Zhao, W.X.; Cheng, M.; Chau, K.T.; Cao, R.W.; Ji, J.H. Remedial injected-harmonic-current operation of redundant flux-switching permanent-magnet motor drives. *IEEE Trans. Ind. Electron.* **2013**, *60*, 151–159. [[CrossRef](#)]
15. Zhu, Z.Q.; Chen, J.T. Multiphase Advanced flux-switching permanent magnet brushless machines. *IEEE Trans. Magn.* **2010**, *46*, 1447–1453. [[CrossRef](#)]
16. Zhang, J.; Cheng, M.; Chen, Z. Investigation of a new stator interior permanent magnet machine. *IET Electr. Power Appl.* **2008**, *2*, 77–87. [[CrossRef](#)]
17. Xue, X.H.; Zhao, W.X.; Zhu, J.H.; Liu, G.H.; Zhu, X.Y.; Cheng, M. Design of five-phase modular flux-switching permanent-magnet machines for high reliability applications. *IEEE Trans. Magn.* **2013**, *49*, 3941–3944. [[CrossRef](#)]
18. Zhang, G.; Hua, W.; Cheng, M. Steady-state characteristics analysis of hybrid-excited flux-switching machines with identical iron laminations. *Energies* **2015**, *8*, 12898–12916. [[CrossRef](#)]

19. Ji, J.H.; Yan, S.J.; Zhao, W.X.; Liu, G.H.; Zhu, X.Y. Minimization of cogging force in a novel linear permanent-magnet motor for artificial hearts. *IEEE Trans. Magn.* **2013**, *49*, 3901–3904. [[CrossRef](#)]
20. Min, W.; Chen, J.T.; Zhu, Z.Q.; Zhu, Y.; Zhang, G.; Duan, G.H. Optimization and comparison of novel E-Core and C-Core Linear switched flux PM machines. *IEEE Trans. Magn.* **2011**, *47*, 2134–2141. [[CrossRef](#)]
21. Cao, R.W.; Cheng, M.; Chris, M.; Hua, W.; Wang, X.; Zhao, W.X. Modeling of a complementary and modular linear flux-switching permanent magnet motor for urban rail transit applications. *IEEE Trans. Energy Convers.* **2012**, *27*, 489–497. [[CrossRef](#)]
22. Wang, C.F.; Shen, J.X.; Wang, Y.; Wang, L.L.; Jin, M.J. A new method for reduction of detent force in permanent magnet flux-switching linear motors. *IEEE Trans. Magn.* **2009**, *45*, 2843–2846. [[CrossRef](#)]
23. Krop, D.C.J.; Encica, L.; Lomonova, E.A. Analysis of a novel double sided flux switching linear motor topology. In Proceedings of the 2010 International Conference on Electrical Machines (ICEM), Rome, Italy, 6–8 September 2010; pp. 1–5.



© 2017 by the authors. Licensee MDPI, Basel, Switzerland. This article is an open access article distributed under the terms and conditions of the Creative Commons Attribution (CC BY) license (<http://creativecommons.org/licenses/by/4.0/>).